Journal of Medical Imaging

MedicalImaging.SPIEDigitalLibrary.org

Segmentation of biological images containing multitarget labeling using the jelly filling framework

Neeraj J. Gadgil
Paul Salama
Kenneth W. Dunn
Edward J. Delp

SPIE.

Neeraj J. Gadgil, Paul Salama, Kenneth W. Dunn, Edward J. Delp, "Segmentation of biological images containing multitarget labeling using the jelly filling framework," *J. Med. Imag.* **5**(4), 044006 (2018), doi: 10.1117/1.JMI.5.4.044006.

Segmentation of biological images containing multitarget labeling using the jelly filling framework

Neeraj J. Gadgil,[a] Paul Salama,[b] Kenneth W. Dunn,[c] and Edward J. Delp[a,*]
[a]Purdue University, Video and Image Processing Laboratory, School of Electrical and Computer Engineering, West Lafayette, Indiana, United States
[b]Indiana University-Purdue University, Indianapolis (IUPUI), School of Electrical and Computer Engineering, Indianapolis, Indiana, United States
[c]Division of Nephrology, Indiana University, School of Medicine, Indianapolis, Indiana, United States

Abstract. Biomedical imaging when combined with digital image analysis is capable of quantitative morphological and physiological characterizations of biological structures. Recent fluorescence microscopy techniques can collect hundreds of focal plane images from deeper tissue volumes, thus enabling characterization of three-dimensional (3-D) biological structures at subcellular resolution. Automatic analysis methods are required to obtain quantitative, objective, and reproducible measurements of biological quantities. However, these images typically contain many artifacts such as poor edge details, nonuniform brightness, and distortions that vary along different axes, all of which complicate the automatic image analysis. Another challenge is due to "multitarget labeling," in which a single probe labels multiple biological entities in acquired images. We present a "jelly filling" method for segmentation of 3-D biological images containing multitarget labeling. Intuitively, our iterative segmentation method is based on filling disjoint tubule regions of an image with a jelly-like fluid. This helps in the detection of components that are "floating" within a labeled jelly. Experimental results show that our proposed method is effective in segmenting important biological quantities. [DOI: 10.1117/1.JMI.5.4.044006]

Keywords: image segmentation; biomedical imaging; fluorescence microscopy; multitarget labeling.

Paper 18127R received Jun. 14, 2018; accepted for publication Nov. 5, 2018; published online Nov. 23, 2018.

1 Introduction

Biomedical imaging modalities are important for understanding biological structures and functions. Recent developments in optical sectioning techniques and specimen preparation have made it possible to collect high-resolution images deep in biological tissues.[1–3] This has enabled researchers to characterize large-scale structures at subcellular resolution and study various biological processes and mechanisms involving them.

Due to the size and complexity of this data, manual analysis becomes impractical. Automatic methods are required for quantitative, objective, and reproducible outcomes.[4,5] However, fluorescence images collected from biological specimens present numerous challenges to automated methods of image analysis. Such images are typically anisotropic and with a variety of aberrations.[6,7] The distortions in such images vary along the different axes such that images from deeper parts of a tissue contain a higher amount of distortions. For images taken successively in the z-direction (or depth) by shifting the focal plane deeper in the sample, image contrast decreases with depth. This reduced contrast worsens a common problem of fluorescence of having very low signal levels consisting of as little as a single photon.[8] Biological samples are typically labeled with multiple probes such that each spectral channel of an image represents fluorescence of a specific probe that chemically binds a certain biological entity in the sample. When one probe labels multiple such entities, one color channel represents two or more structures (or multiple targets), which we call "multitarget labeling." The challenge here is to automatically detect and quantify these structures separately.[9] Also, the color channel isolation is often imperfect causing crosstalk between different spectral channels.[6] In *in-vivo* imaging, motion artifacts are introduced as a result of respiration and heartbeat of the live specimen.[10]

In the past years, several image processing techniques have been developed for segmenting and analyzing biological images. Edge detection methods proposed by Canny[11] and Harris[12] are widely used for segmenting boundaries of biological quantities. Primary image processing methods, such as thresholding,[13] morphological operations,[14,15] and 2-D/3-D filters with various kernels,[16] are used as preprocessing to remove noise and distortions and to binarize images before doing segmentation.

Active contours (also known as snakes) is a widely used segmentation approach.[17,18] In principle, an active contour is a curve that evolves within an image from some initial position toward the boundary of the biological object. The evolution of the snake is formulated as a minimization problem and its associated cost function is usually referred to as snake energy. Edge-based active contours[17,19] compute an image gradients map to identify objects. Snakes has been investigated using region-based approaches, seeking an energy equilibrium between the foreground and the background.[20] The region-based methods can typically produce better segmentation results than the edge-based methods. Yet, they fail to segment images with inhomogeneous intensities.[21] Stochastic active contour scheme (STACS) is another popular technique that uses textures, edge, and region-based information.[22] A topology-preserving active contour method that uses image topology with "level-set formulation" is developed in Ref. 23. Other variants of STACS include a method based on vector field convolution[24]

*Address all correspondence to: Edward J. Delp, E-mail: ace@ecn.purdue.edu

2329-4302/2018/$25.00 © 2018 SPIE

and an open active contour model developed to analyze actin filament.[25] A 3-D extension to this concept known as active surfaces is proposed in Ref. 7 that considers images as a 3-D volume using modified energy functions. Despite a large amount of work that has been presented on active contour and its variations, this approach still suffers from many limitations and shortcomings, such as its high sensitivity to initial curves, noise, bias field, nonuniform image contrast, and its inability to discriminate multiple biological objects.[18,26]

Watershed technique is another popular segmentation approach based on mathematical morphology.[27] Many variations of this approach have been proposed over the years. A seeded watershed method makes use of "seeds" as the pixels used for initializing regions.[28] Another method presented in Ref. 29 uses prior probabilistic information with the watershed transform. A two-step watershed method is presented in Ref. 30. In this method, three types of cell structures: nuclei, cell walls, and cell-to-cell contacts are segmented in order to distinguish different actin-binding proteins from the images of epithelial cells. Although watershed variants are widely used for image analysis for various applications, they typically tend to oversegment quantities in biological images, resulting into thousands of small basins.[29] Like active contours, watershed methods are also highly sensitive to image noise. Also, watershed typically produces bad segmentation results in low contrast and poor edge-areas that are typical in microscopy images. To address the oversegmentation issue, the use of a marker image is described in Ref. 31, which claims to reduce the number of minima in an image. The use of anisotropic filters[32] has been proposed to alleviate image noise.

Active mask framework that uses region-based and voting-based function with multiscale and multiresolution capability is proposed in Ref. 33. A region-partition method called discrete region competition is proposed in Ref. 34. A sliding band filter-based joint segmentation approach presented in Ref. 35, that is useful in detecting overall convex shapes. To segment vasculature in 3-D, a technique that uses noise modeling, planer geometry, and adaptive region growing is presented in Ref. 36. A approach for coupling image restoration-segmentation[37] has been proved effective in segmenting 3-D biological structures, e.g., the endoplasmic reticulum and the Drosophila wing disc. This approach uses noise modeling, planer geometry to detect candidate voxels, followed by an adaptive region growing scheme to segment weakly labeled vessels. In Ref. 38, a statistical point process-based approach is applied to segment biological objects that can be modeled with shape parameters, such as cellular nuclei. A popular edge and ridge-based method that uses steerable filters for feature detection is proposed in Ref. 39. Many of these methods are developed to fulfill specific image analysis goals for particular type of images.

Many learning-based methods have been developed for medical image analysis. This includes many data-driven convolutional neural network (CNN)-based approaches, such as deep learning, that have been recently developed and proven successful for the analysis of mammograms, cardiovascular, and microscopy images.[40] An efficient deep contour-aware network is proposed to automatically segment glands from histology images, under a unified multitask learning framework.[41] A multiple instance learning-based framework that is designed using a CNN architecture to analyze mammalian and yeast datasets is presented in Ref. 42. Most such methods need some amount of prior training, which involves using the ground truth information.[43] In many imaging-based experiments, such as *in-vivo* fluorescence microscopy, ground truth is impossible to obtain since both the shape and position of an object are fluid in living animals and are inevitably altered in the process of isolating and fixing tissues.[7] To obtain hand-segmented results from an expert clinician for multiple 3-D volumes to be used as the training data, it becomes significantly difficult and tedious.

Figure 1 shows some examples of our image data. Figures 1(a) and 1(b) show single focal plane images collected from fixed rat kidney tissue labeled with rhodamine-phalloidin using multiphoton microscopy. The two images, which were collected at different depths, show phalloidin labeling of both the basement membrane of proximal tubules (outlining the tubule boundaries) as well as the brush borders that extend into the tubule lumens. Here, our first image analysis goal is to segment the tubule boundaries for measuring tubule diameter or volume. Second, it is also intended to isolate the brush border of the tubule lumens for measuring the volume of the brush border. Figure 1(c) shows an example of a single channel of images taken from a rat liver such that the fluorescent probe labels cell boundaries and endothelia. The segmentation goal here is to highlight blood vessels and cell–cell junctions, in order to quantitatively characterize the vascular space and hepatocytes. Figure 1(d) shows an example of DCE-MRI breast images taken using the TWIST Dixon pulse sequence technique.[44] It is intended that breasts from the images are highlighted and isolated from the body. It is also desired to quantify fat versus fibroglandular tissue inside each breast. Each type of above data thus contains a single probe labeling multiple biological entities or targets that need to be discriminated based on their 3-D structural properties.

We earlier proposed a "jelly filling" segmentation approach that can segment separable biological entities characterized by closed shapes outlined by their boundaries.[9] In this paper, we

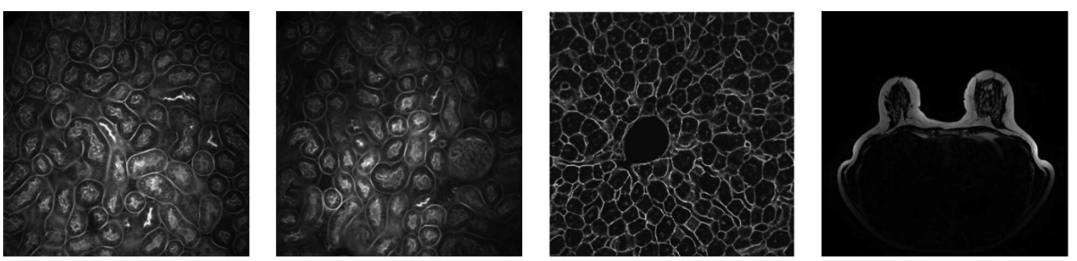

Fig. 1 Examples of our image data. (a), (b) Rat kidney tissue image, (c) rat liver image, and (d) DCE-MRI breast image. Images (a), (b), and (c) were obtained using taken using multiphoton microscopy, and (d) was obtained using TWIST Dixon pulse sequence technique.

extend our previous method by doing motion-compensation for the images used for the z-direction correction and by improving the stopping criterion. We provide further results for kidney, liver, and mammogram images. We present a comparison of the results obtained using our proposed method and some existing segmentation methods in terms of visual and objective analysis. We also present a preliminary analysis of the iterative behavior of our proposed method, indicating a stable convergence. Note that we call the outer encapsulations (i.e., tubule, cell, breasts) simply "boundaries" and the inside remains (i.e., brush borders, endothelia/vascular space, breast tissues) "lumen" throughout the description of our method. An overview of our approach is presented next.

2 Overview of Our Approach

As shown in Fig. 2, we first use adaptive thresholding on the original grayscale images to produce binary images. (The fluorescence microscopy images collected from rat kidneys and livers typically consist of two channels that reflect the fluorescence of the two probes added to the tissue. We first separate the color channel corresponding to the probe used to label multiple biological targets, to obtain grayscale images.) Adaptive thresholding is effective in dealing with radial intensity drop in an image because a local statistic is used as a threshold to segment each pixel as foreground/background. To be able to separate boundaries and lumen, we use an iterative segmentation approach that aims to detect "floating" elements inside the disjoint regions corresponding to biological encapsulations, such as tubules, liver cells, or breasts. Intuitively, our method is based on filling a disjoint region of an image with a "jelly-like" fluid with a unique label. This helps in the detection of components that are floating within a "labeled-jelly." The "viscosity" of the jelly can be controlled using simple morphological operations, such as erosion and dilation using a specific structural element.[15,45] The images generally have a lower sampling rate in the z-direction and lumen cannot be typically separated as a completely separate 3-D component from the tubule boundaries. Therefore, instead of using a 3-D component analysis, we use a 2-D component analysis to detect a part of lumen as a floating component in an image and then use it to "correct" the segmented images from the adjacent focal planes, consequently improving the 3-D segmentation. To account for *in-vivo* specimen movement (such as due to respiration or heartbeat), motion compensation is done to align subsequent 2-D segmented images, prior to the correction. We express this correction mathematically as "motion-compensated z-series consistency potential." We also use a 2-D "neighborhood voting potential" to consider the effect of neighboring segmented pixels and define a clear separation between the boundary and lumen regions. This approach is conceptually based on region-growing techniques, such as the one mentioned in Refs. 33 and 34. In each iteration, each pixel is segmented/classified as either belonging to "boundary" or "lumen" using a potential function that considers the influence of the above mentioned factors. This process is repeated until the relative change (expressed as a percentage) in pixel classification decreases below a fixed level for each image. Details of the proposed segmentation method are provided next.

3 Jelly Filling Segmentation

Let $\mathcal{I}_{z_p}$, $p = \{1, 2, \ldots, P\}$ be the grayscale input images for our segmentation method, where p indicates the index of the focal plane from which an image is collected. P is the total number of images collected from one 3-D biological sample. Let $\mathcal{S}_{Th,z_p}$ denote the binary images after adaptive thresholding. The iterative segmentation process begins with an initial configuration of boundaries and lumen denoted by $\psi^{(i)}_{B,z_p}$ and $\psi^{(i)}_{L,z_p}$, respectively. Let $\psi^{(k)}_{B,z_p}$ and $\psi^{(k)}_{L,z_p}$ denote, respectively, the configuration of "boundaries" and "lumen," obtained from $\mathcal{I}_{z_p}$, after the k'th ($k = 1, 2, 3, \ldots$) iteration. The final segmented configurations of $\mathcal{I}_{z_p}$ are denoted by $\psi^{(f)}_{B,z_p}$ and $\psi^{(f)}_{L,z_p}$. A pixel from an image is denoted by s. Now, we describe each step of our proposed jelly filling segmentation.

3.1 *Adaptive Thresholding*

The main purpose of this step is to separate the foreground that represents the presence of a biological structure. To do this, we use an adaptive thresholding scheme that uses 3-D neighborhood information. In particular, let the $w_1 \times w_2 \times w_3$ 3-D window (Ω_{Th}) centered at pixel s and let $\tau_{z_p}(s)$ be the mean pixel intensity of the neighborhood Ω_{Th}. The local mean $\tau_{z_p}(s)$ is used as the corresponding threshold for s as indicated by Eq. (1) below and $\mathcal{I}_{z_p}(s)$ is used to denote the intensity of the pixel at location s within the volume $\mathcal{I}$:

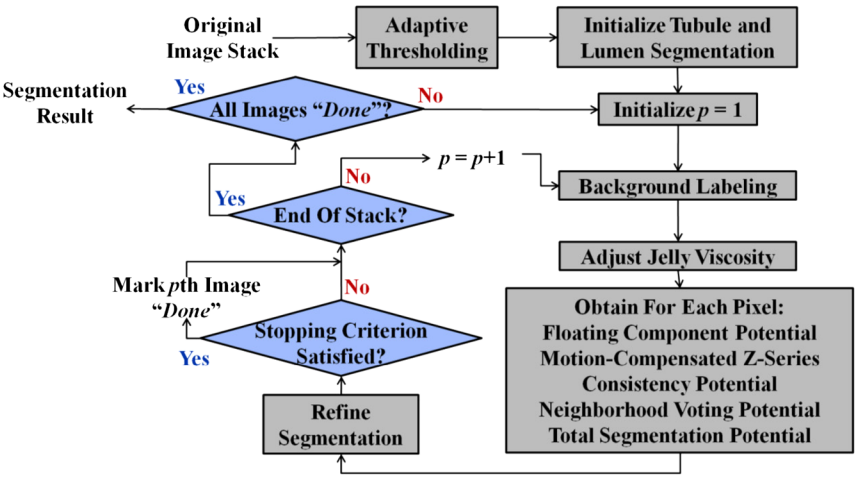

Fig. 2 Flow chart of the proposed approach.

$$\mathcal{S}_{Th,z_p}(s) = \begin{cases} 1 & \text{if } \mathcal{I}_{z_p}(s) \geq \tau_{z_p}(s) \\ 0 & \text{if } \mathcal{I}_{z_p}(s) < \tau_{z_p}(s) \end{cases}. \quad (1)$$

We use the outcome of this step as our initial segmentation. For the p'th image, we set $\psi^{(0)}_{B,z_p} = S_{Th,z_p}$ and $\psi^{(0)}_{L,z_p} \equiv 0$, i.e., all pixels that exceed their corresponding thresholds are initially labeled as belonging to boundaries. This also contains the pixels belonging to lumen, which are separated from the boundaries in the subsequent steps of our iterative framework.

3.2 *Background Labeling*

This step separates the disjoint background regions from the output of the adaptive thresholding and assigns them with different labels. Because of the underlying biological structure, the background is composed of regions belonging to different biological compartments that can be separated into disjoint sets of pixels. Intuitively, this can be viewed as filling these disjoint compartments (or encapsulated regions) with a "jelly-like" fluid. The viscosity of this fluid reflects into the pixel neighborhood used for finding disjoint regions of the background.

Consider a boundary configuration $\psi^{(k-1)}_{B,z_p}$ resulting from the $(k-1)$'th iteration. $\psi^{(k-1)}_{B,z_p}$ is used as the starting configuration for k'th iteration. Let $\Lambda^{(k)}_{z_p}$ denote the background image the k'th iteration. $\Lambda^{(k)}_{z_p}$ is derived from $\psi^{(k-1)}_{B,z_p}$ as follows:

$$\Lambda^{(k)}_{z_p} = \{s | \psi^{(k-1)}_{B,z_p}(s) = 0\}. \quad (2)$$

Let us assume that there are M disjoint background regions in $\Lambda^{(k)}_{z_p}$. Each such disjoint background region is labeled as $\lambda^{(k)}_{m,z_p}$, such that

$$\Lambda^{(k)}_{z_p} = \bigcup_{m=1,2,\ldots M} \lambda^{(k)}_{m,z_p}, \quad (3)$$

and each $\lambda^{(k)}_{m,z_p}$ represents a group of pixels belonging to the biological entity enclosed by the boundary. Each $\lambda^{(k)}_{m,z_p}$ is obtained using the connected component labeling using a four-point neighborhood to $\Lambda^{(k)}_{z_p}$.[16]

3.3 *Segmentation Based on a Potential Function $P(\cdot)$*

The goal is to separate the pixels belonging to lumen from those of boundaries. We consider three factors that influence this separation:

- A pixel belonging to a "floating" component is likely to be segmented as lumen.
- It is important to maintain structural consistency in the z-direction. A motion-compensated segmentation correction in the z-direction is developed to model this factor.
- The effect of segmentation of neighboring pixels of an image needs to be considered to determine whether a pixel belongs to boundaries or lumen.

We consider influence of these factors in terms of values assigned to each pixel, obtained using potential functions each of which corresponds to a factor. The total potential is the summation of these individual potentials, such that the sign of this summation determines whether a pixel is classified as boundary or lumen. For each p'th image I_{z_p}, $\psi^{(k)}_{B,z_p}$ and $\psi^{(k)}_{L,z_p}$ are updated based on $\mathcal{S}_{Th,z_p}$ and a potential function $P(\cdot)$.

Pixels classified as background pixels are not considered to be a part of either boundary or lumen. Thus,

$$\psi^{(k)}_{B,z_p}(s) = \psi^{(k)}_{L,z_p}(s) = 0 \quad \text{for all } s \notin \mathcal{S}_{Th,z_p}. \quad (4)$$

Next, $P^{(k)}_{z_p}(s)$ is obtained for only the pixels s, where $\mathcal{S}_{Th,z_p}(s) = 1$. Based on the sign of $P(s)$, each pixel s is assigned to be either a member of boundaries $\psi^{(k)}_{B,z_p}$ or lumen $\psi^{(k)}_{L,z_p}$ according to

$$\psi^{(k)}_{B,z_p}(s) = \begin{cases} 1 & \text{if } s \in \mathcal{S}_{Th,z_p} \text{ and } P^{(k)}_{z_p}(s) \leq 0 \\ 0 & \text{otherwise} \end{cases} \quad (5)$$

and

$$\psi^{(k)}_{L,z_p}(s) = \begin{cases} 1 & \text{if } s \in \mathcal{S}_{Th,z_p} \text{ and } P^{(k)}_{z_p}(s) > 0 \\ 0 & \text{otherwise} \end{cases}. \quad (6)$$

Now, $P^{(k)}_{z_p}(s)$ is the sum of three components: $P^{(k)}_{F,z_p}(s)$, floating component potential; $P^{(k)}_{M,z_p}(s)$, motion compensated z-series consistency potential; and $P^{(k)}_{N,z_p}(s)$, neighborhood voting potential. In sum:

$$P^{(k)}_{z_p}(s) = P^{(k)}_{F,z_p}(s) + P^{(k)}_{M,z_p}(s) + P^{(k)}_{N,z_p}(s). \quad (7)$$

Note that $P(\cdot)$, $P_F(\cdot)$, $P_M(\cdot)$, and $P_N(\cdot)$ are defined only for all pixels s, such that $\mathcal{S}_{Th,z_p}(s) = 1$. Henceforth, we will assume $\mathcal{S}_{Th,z_p}(s) = 1$ for all future references to s, unless specified otherwise.

3.3.1 *Floating component potential $P_F(\cdot)$*

This potential represents identifying a component that is "floating" in one background region and labeling it as lumen. A floating component is defined as a connected component with only one label surrounded by the background. To obtain the floating component potential during iteration k, we consider $\psi^{(k-1)}_{B,z_p}$, the configuration of boundaries from the $(k-1)$'th iteration, and $\lambda^{(k)}_{m,z_p}$ for $m = 1, 2, \ldots, M$, the disjoint background regions, as described earlier. Let C denote the set of all connected components in $\psi^{(k-1)}_{B,z_p}$ obtained using four-pixel neighborhood connectivity. Each $c \in C$ is a set of pixels belonging to a single connected component. The outer boundary of each c, denoted by b_c, is next found by selecting the boundary pixels of the morphological dilation of c using the same structural element used to account for the viscosity of the jelly. Also, let C_F ($C_F \subseteq C$) denote the set of all floating components, that is

$$C_F = \{c | b_c \subseteq \lambda^{(k)}_{l,z_p}, \text{ for some } l \in \{1, 2, \ldots, M\}\}. \quad (8)$$

Now, we assign floating point potential (P_F) to each pixel s as follows:

$$P^{(k)}_{F,z_p}(s) = \begin{cases} \alpha_f & \text{if } s \in C_F \\ -\alpha_f & \text{otherwise} \end{cases}, \quad (9)$$

where α_f is a positive constant, whose value is chosen in such a way so as to influence the labeling of floating components as lumen.

3.3.2 *Motion-compensated z-series consistency potential* $P_M(\cdot)$

While iteratively processing the images from successive focal planes, it is important to maintain structural continuity in all directions. This can be accomplished if the segmentation of neighboring images along the z-direction influences the segmentation of current image. To do this, we use w_Z boundary configurations in either direction along the z-axis (total of $2 \times w_Z$ images) from the previous, i.e., $k-1$'th iteration: $\psi^{(k-1)}_{B,z_{p+n}}$, $n \in \{-w_Z, \ldots, -1, 1, \ldots, w_Z\}$. Each of these configurations is first motion compensated with respect to the p'th image ($\psi^{(k-1)}_{B,z_p}$) to counter any movement of the specimen while imaging *in-vivo* or other imaging effects that vary from one focal plane to another.

We do motion compensation for each $\psi^{(k-1)}_{B,z_{p+n}}$ individually, using only $\psi^{(k-1)}_{B,z_p}$ as the reference image. Let $\psi^{(k-1)\{MC\}}_{B,z_{p+n}}$ be the motion-compensated boundary configurations derived from the corresponding original $\psi^{(k-1)}_{B,z_{p+n}}$ for $n \in \{-w_Z, \ldots, -1, 1, \ldots, w_Z\}$ by selecting the minimum sum of absolute difference (SAD) translational motion among the motion candidates from a square window Ω_{MC} a ($\pm w_{MC} \times \pm w_{MC}$) centered around the origin.

First, (m_x, m_y) the translational motion in the x-and the y-direction is obtained using the minimum-SAD:

$$(m_x, m_y) = \underset{(m^c_x, m^c_y) \in \Omega_{MC}}{\arg\min} \sum_{\text{All Pixels}} |\psi^{(k-1)}_{B,z_{p+n}}(s_x + m^c_x, s_y + m^c_y) - \psi^{(k-1)}_{B,z_p}(s_x, s_y)|, \tag{10}$$

where (s_x, s_y) represents the $x-y$ indices of pixel s.

Then, we compute the corresponding motion compensated boundary and lumen configurations: $\psi^{(k-1)\{MC\}}_{B,z_{p+n}}$ and $\psi^{(k-1)\{MC\}}_{L,z_{p+n}}$, respectively:

$$\psi^{(k-1)\{MC\}}_{B,z_{p+n}}(s_x, s_y) = \psi^{(k-1)}_{B,z_{p+n}}(s_x + m_x, s_y + m_y), \tag{11}$$

$$\psi^{(k-1)\{MC\}}_{L,z_{p+n}}(s_x, s_y) = \psi^{(k-1)}_{L,z_{p+n}}(s_x + m_x, s_y + m_y). \tag{12}$$

Now, we employ a one-dimensional (1-D) Gaussian function of length $(2w_z + 1)$: $f_z(n) = [1 - \delta(n)] \cdot e^{-\frac{|n|^2}{2^2}}$, $n = -w_z, \ldots, 0, \ldots, w_z$ and define $P_z(s)$ to be as follows:

$$P^{(k)}_{M,z_p}(s) = \sum_{n=-w_z}^{w_z} \{\psi^{(k-1)\{MC\}}_{L,z_{p+n}}(s) - \alpha_z \cdot \psi^{(k-1)\{MC\}}_{B,z_{p+n}}(s)\} \cdot f_z(n), \tag{13}$$

where α_z is a constant whose value is set to provide suitable z-series consistency for boundary and lumen classification.

3.3.3 *Neighborhood voting potential* $P_N(\cdot)$

To clearly define the separation between boundary and lumen segments, a 2-D Gaussian voting function is used. It is conceptually similar to the voting-based distributing function used in the active mask framework.[33] We define $P_n(s)$ to be as follows:

$$P^{(k)}_{N,z_p}(s) = \{(\psi^{(k-1)}_{L,z_p} - \psi^{(k-1)}_{B,z_p}) * f_n\}(s), \tag{14}$$

where * represents 2-D convolution and f_n is a truncated 2-D Gaussian function of size $(2w_n + 1) \times (2w_n + 1)$:

$$f_n(x, y) = \frac{1}{F_{w,n}} \cdot e^{-\frac{(|x|^2 + |y|^2)}{2^2}}, \qquad x, y = -w_n, \ldots, 0, \ldots, w_n, \tag{15}$$

where $F_{w,n} = \sum_{i_n=-w_n}^{w_n} \sum_{j_n=-w_n}^{w_n} e^{-\frac{(|i_n|^2 + |j_n|^2)}{2^2}}$.

3.4 *Morphological Operations*

In order to adjust the viscosity of the jelly or the background ($\Lambda^{(k)}_{z_p}$), we use morphological opening to the original background image using a circular structuring element.[45] To preserve a high-level structural continuity, tiny clusters of connected pixels can be safely removed from a segmentation configuration.

Algorithm 1: Jelly filling segmentation

Require: Input images $\mathcal{I}_{z_p}$, $p = 1, 2, \ldots, P$

Do **Adaptive Thresholding** to $\mathcal{I}_{z_p}$ to obtain $\mathcal{S}_{Th,z_p}$ for $p = 1, 2, \ldots, P$

Initialize: $\psi^{(i)}_{B,z_p} = \psi^{(0)}_{B,z_p} = S_{Th,z_p}$, $\psi^{(i)}_{L,z_p} = \psi^{(k)}_{L,z_p} \equiv 0$ for $p = 1, 2, \ldots, P$

Initialize $k = 0$ to begin the iterative process

while (All images are not done) **do**

  for Each pth image **do**

    Do **Morphological Opening** of the background $\Lambda^{(k)}_{z_p}$ to account for the viscosity of the "jelly"

    Clean-up: Remove small components of $\Lambda^{(k)}_{z_p}$ ($<\gamma$ pixels)

    Do **Background Labeling** using 4-pixel neighborhood

    for Each pixel s such that $\mathcal{S}_{Th,z_p}(s) = 1$ **do**

      Obtain **Floating Component Potential** $P^{(k)}_{F,z_p}(s)$ using α_f

      Obtain **Motion-Compensated Z-Series Consistency Potential** $P^{(k)}_{M,z_p}(s)$ using α_z, w_z, w_{MC}

      Obtain **Neighborhood Voting Potential** $P^{(k)}_{N,z_p}(s)$ using w_n

      Obtain **Potential Function** $P^{(k)}_{z_p}(s)$ using $P^{(k)}_{F,z_p}(s)$, $P^{(k)}_{M,z_p}(s)$ and $P^{(k)}_{N,z_p}(s)$

      Do segmentation to get $\psi^{(k)}_{B,z_p}(s)$ and $\psi^{(k)}_{L,z_p}(s)$

    Clean-up: Remove small components of $\psi^{(k)}_{B,z_p}$ ($<\gamma$ pixels)

    Compute the change in pixels $\Delta^{(k)}_{z_p}$

    if Stopping Criterion Υ is satisfied: $\Delta^{(k)}_{z_p} < \epsilon$ **then**

      Declare pth image is done

    Increment k to go to the next iteration

  for Each pth image **do**

    Assign $\psi^{(f)}_{B,z_p}$ and $\psi^{(f)}_{L,z_p}$ as boundary and lumen segmentation configurations obtained in the last iteration.

We call this operation "clean-up," such that the values of pixels belonging to components smaller than γ pixels are assigned to 0.

3.5 *Stopping Criterion*

As stated above, we use percentage change in number of boundary pixels as the stopping criterion. In particular, we define as follows:

$$\Delta_{z_p}^{(k)} = \frac{\text{Diff}(\psi_{B,z_p}^{(k)}, \psi_{B,z_p}^{(k-1)})}{\text{Total pixels}} \times 100, \tag{16}$$

where Diff indicates the number of changed pixels, that is $\text{Diff}(A, B) = \sum_{\text{All pixels}} (A \text{ XOR } B)$. The stopping criterion is as follows:

$$\Upsilon\text{: Is } \Delta_{z_p}^{(k)} < \epsilon \text{ for every } p? \tag{17}$$

The steps of our proposed segmentation method are outlined in Algorithm 1.

4 Experimental Results

We implemented jelly filling segmentation using MATLAB. An ImageJ[46] plugin is currently under development.

4.1 *Image Datasets*

For our experiments, we mainly used images obtained using two-photon microscopy of rat samples. The first type of image data (K-I, K-II, K-III, and K-IV) is in total 599 kidney images obtained using fluorescence microscopy. Each image is of 512×512 pixel, containing 8-bit data from three-color channels. (K-I was provided by Malgorzata Kamocka of Indiana University and was collected at the Indiana Center for Biological Microscopy. K-II, K-III, and K-IV were provided by Tarek Ashkar of the Indiana University Division of Nephrology.) Images from K-I were taken from a rat kidney and labeled with TexasRed-phalloidin. Images from K-II, K-III, and K-IV were taken from a mouse kidney and labeled with Alexa488-phalloidin. The fluorescence of phalloidin (which labels filamentous actin) labeled multiple structures in the tissue, the basement membrane of the tubules, the brush border of the proximal tubules, and the glomeruli.

The second type of images is of rat liver samples. Liver datasets L-I, L-II, L-III, L-IV, L-V, L-VI, and L-VII each contained 8-bit, three-color channels, images (512×512 pixel dimensions) of rat liver specimen obtained using fluorescence microscopy. Overall, L-I-L-VII consists of 44 images. (The liver data were provided by Sherry Clendenon and James Sluka of the Biocomplexity Institute, Indiana University at Bloomington.) The liver samples are labeled with a fluorescent tomato lectin, which labels cell boundaries and endothelia.

We also used a third type of data that is composed of DCE-MRI breast images that use the TWIST Dixon pulse sequence technique.[44] This data consisted of four sets (M-I, M-II, M-III, and M-IV) each of 128 grayscale mammograms of 512×512 pixel dimensions. (The mammography data was provided by Yuan Le, Randall Kroeker, Hal Kipfer, and Chen Lin and was collected at the Department of Radiology and Imaging Science, Indiana University.) The bright regions in these images represent breast regions with tissues. The goal here is to highlight breast regions and isolate and quantify fat versus fibroglandular tissue inside each breast.

4.2 *Parameter Selection*

We now discuss the selection of parameters, which are summarized in Table 1 for convenience.

- α_f and α_z: We aim to provide a stable final configuration that undergoes practically negligible changes in boundary and lumen configurations after reaching the stopping criterion. In particular, the parameters α_f and α_z should be selected such that a right balance among the potentials is maintained. Note that the sum of different potentials is positive, which means we classify the component to be lumen, otherwise it is boundary. We choose the initial configuration "all boundaries." As the value of α_f increases, the floating components are more likely to be classified as lumen. In our experiments, we chose $\alpha_f = 1$ and tested that a positive value between $0 < \alpha_f \leq 2$ gives reasonable results. As α_z increases, the influence of the boundary-segmented z-series pixels increases that makes pixels more likely to be classified as boundary. So, the value of α_z needs to be positive but <1. A value close to 1 means that the pixel is highly likely to be classified as boundary and the final result may resemble the initial "all-boundaries" configuration. Setting $\alpha_z \approx 0$ reduces the effect of the boundaries from the z-series may cause the undesired "all lumen" configuration. We used $\alpha_z = 0.25$ to set a reasonable balance with $\alpha_f = 1$ and a desired range of α_z was found experimentally to be $0.1 \leq \alpha_z \leq 0.9$.
- Window lengths w_1, w_2, w_3, w_z, w_{MC}, and w_n are determined empirically, as shown in Table 1. Some of these may need to be changed based on image-dimensions and other image properties, such as motion, noise etc. For example, the motion search window is typically between $1 \leq w_{MC} \leq 10$, where a higher value indicates a larger motion-search neighborhood at the cost of a higher false motion and more computations.
- ϵ represents the percentage pixel change for stopping the iterative process. A higher value would mean stopping at

Table 1 Parameters used for our experiments.

Parameter	Description	Value	Ref. range
α_f	Floating influence	1	$0 < \alpha_f \leq 2$
α_z	Z-series influence	0.25	$0.1 \leq \alpha_z \leq 0.9$
w_1, w_2, w_3	Thresholding window	15, 15, 3	–
w_z	Z-series window	2	$1 \leq w_z \leq 5$
w_{MC}	Motion-search window	5	$1 \leq w_{MC} \leq 10$
w_n	Neighborhood window	2	$1 \leq w_n \leq 5$
γ	Clean-up threshold	50	$10 \leq \gamma \leq 100$
ϵ	Stopping criterion	0.1	Typically, 1/0.1

an earlier iteration, which may lead to incomplete segmentation. We use 0.1 in our experiments and $\epsilon = 1$ also gives reasonable outcomes.

- γ is decided empirically to be $10 \leq \gamma \leq 100$ as number of pixels in a cluster to be cleaned-up as noise.

Note that we used the same set of parameter values from the "value" column of Table 1 for our experiments to obtain the segmentation results for all datasets. While it may be possible to obtain better results than we reported by a more involved selection approach, we avoided further fine-tuning since it is not practical to expect it to be done for each application of our method. Our experiments indicated obtaining a stable final segmentation that satisfied the stopping criterion for the corresponding reference range of parameters listed in the last column of Table 1.

4.3 *Illustration*

Figure 3 shows an illustration of our proposed framework using K-I data. Our proposed jelly filling iterative segmentation begins with initial configurations ($k = 0$) for the $p = 112$'th image: $\psi^{(i)}_{B,z_{112}} = S_{Th,z_{112}}$, $\psi^{(i)}_{L,z_{112}} \equiv 0$, where all pixels are segmented as boundaries. For subsequent iterations $k = 1, 2, \ldots,$ intermediate configurations $\psi^{(k)}_{B,z_{112}}$, $\psi^{(k)}_{L,z_{112}}$ are generated until the stopping criterion (Υ) is satisfied. In the example shown, this occurs at $k = 24$, leading to the final segmentation results $\psi^{(f)}_{B,z_{112}} = \psi^{(24)}_{B,z_{112}}$ and $\psi^{(f)}_{L,z_{112}} = \psi^{(24)}_{L,z_{112}}$.

For an iterative method, it is important to address its convergence. Although in our work we do not discuss theoretical convergence, our experiments indicated a stable convergence for a range of parameter values without the need of fine-tuning, which may give even a better performance than reported in this work. We did some preliminary analysis based on the observed percent pixel change in the boundary configuration and the segmentation accuracy at each successive iteration of our proposed method.

First, the iterative process was allowed to run for over 100 iterations for the 40 images that were hand-segmented. In this case, the stopping criterion specified earlier in Eq. (17) was not used. Figure 4(a) shows the percentage of pixels that changed configurations from boundary to lumen at each iteration k, when compared with its immediate previous iteration. The vertical bar at each iteration number indicates the range of % pixel change for all 40 images, whereas the dot represents the average. Recall that our initial configuration (iteration 0) is "all boundaries" (or "no lumen"). There is high positive value of the % pixel change for $k = 1$ because our method has detected many "floating" components that are transfered from boundary configuration to lumen for the first time. For the next few iterations, the

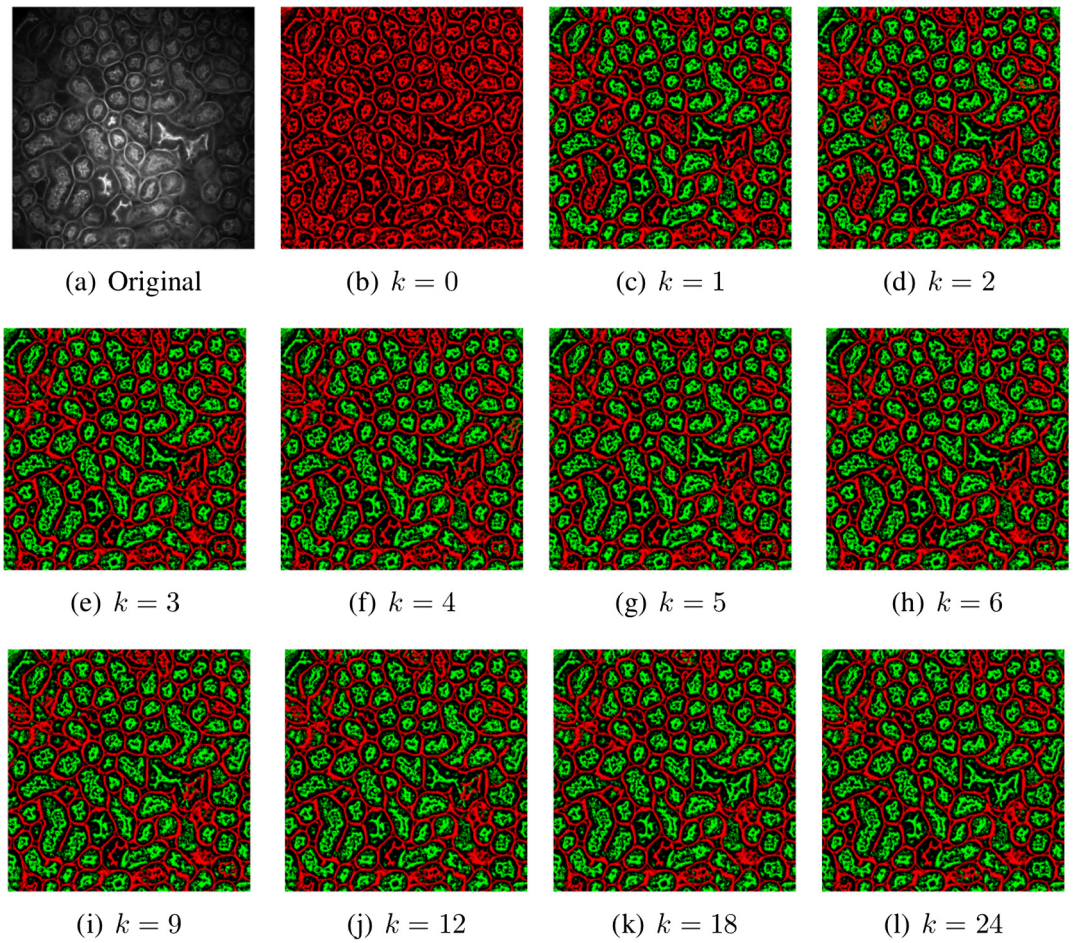

Fig. 3 An illustrative example showing segmentation outcome at various iterations of our proposed method: from $k = 0$ (initialization) to 24 (final) red: boundaries, green: lumen. (a) Original, (b) $k = 0$, (c) $k = 1$, (d) $k = 2$, (e) $k = 3$, (f) $k = 4$, (g) $k = 5$, (h) $k = 6$, (i) $k = 9$, (j) $k = 12$, (k) $k = 18$, and (l) $k = 24$.

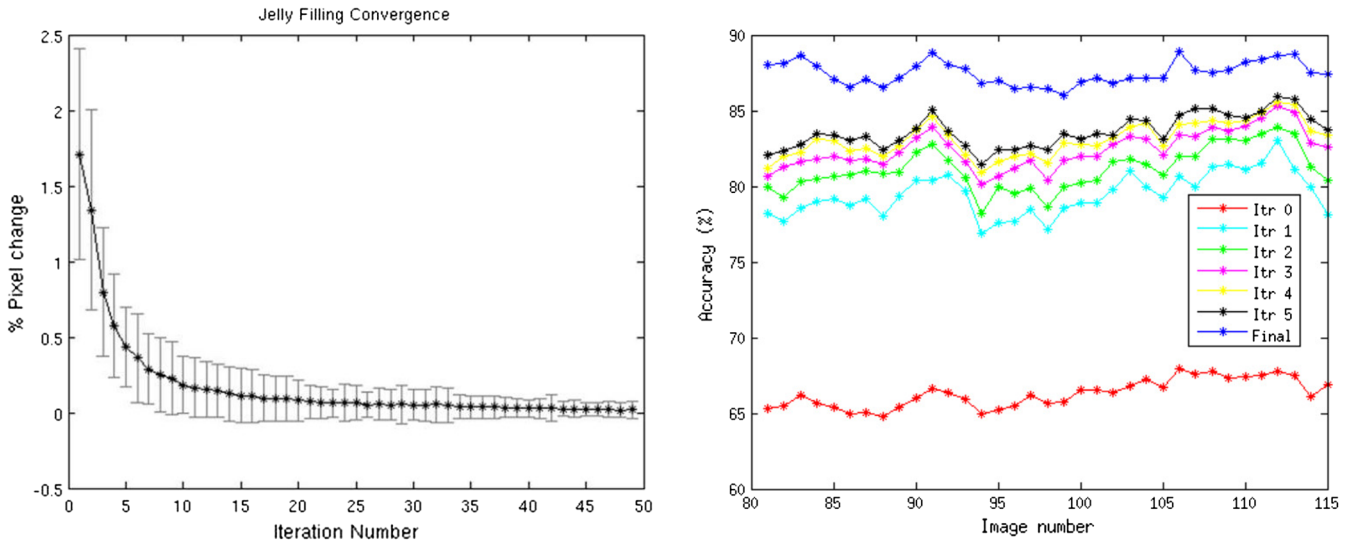

(a) Pixel change percentage (b) Accuracy

Fig. 4 Jelly filling: iterative behavior. (a) Pixel change percentage and (b) accuracy.

pixel change is positive but generally decreasing. This indicates that during each jelly filling iteration, the segmentation configurations are further refined such that more lumen components are detected. Approximately around $k = 15$, for some images, the pixel change becomes negative. This means that more pixels changed from lumen back to boundaries than otherwise. For $k > 35$, the average percent pixel change remains very close to 0 with a small range, indicating that there is no significant change in the boundary and lumen configurations, then on and for practical purposes, we can terminate the iterative process since the differences in the configurations seem to become both statistically and visibly negligible.

Next, we observe the segmentation accuracy for a stack of images after each iteration of our proposed method. Figure 4(b) shows the plot of % accuracy at successive iterations for a set of K-I images, until the process stops producing the final segmentation result. Each color represents a specific iteration (k) of our jelly filling method. $k = 0$ has the lowest accuracy (60% to 70%) since it was "all-boundaries" configuration initialized using the result of adaptive thresholding. This configuration is similar to the results obtained using a typical segmentation method that can discern only a biological entity based on the pixel intensities. There is a significant increase in accuracy from $k = 0$ to $k = 1$ because the first jelly filling iteration has detected many "floating" components that are converted from boundary configuration to lumen. Is can be observed that the accuracy further increases for all images in the subsequent iterations: $k = 2$, 3,4, 5. For $k > 5$, accuracy increases in smaller steps that is not shown here to avoid clutter. When the stopping criterion is satisfied, the final boundary configuration has produced accuracy more than 85% (shown in blue). It is also interesting to note that accuracy changes across images. This suggests that some images are "easy" for our proposed method and they generally help improve the segmentation of the neighboring images, whereas some images are "difficult" representing significant structural discontinuities or noise.

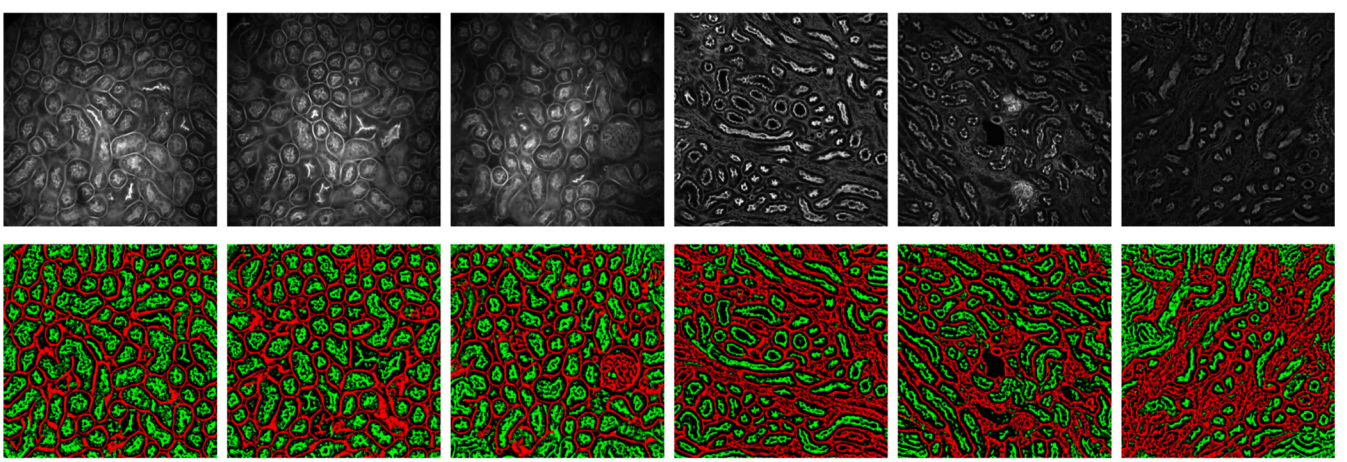

(a) (b) (c) (d) (e) (f)

Fig. 5 Examples of segmentation results for the kidney images, top row: original images, bottom row: boundaries (red) and lumen (green). (a–c) K-I, (d) K-II, (e) K-III, and (f) K-IV.

4.4 *Segmentation Results and Analysis*

Figures 5(a)–5(c) show examples of results using the kidney images from K-I. As it can be observed, most of the tubule boundaries and their corresponding lumen are segmented correctly. There are a few missing tubules mainly near the image-borders and a few falsely detected tubules that should have been classified as lumen. The segmentation errors in the corners are mainly due to low signal levels resulting from vignetting in the images. The segmentation results obtained by our method significantly enhance the ability to visually identify individual contiguous tubules. Figure 5(c) consists of a glomerulus, an important biological entity used for characterizing a nephron of the kidney. Figures 5(d) and 5(e) show images and segmentation results from K-II and K-III, respectively. In these images, many tubules and lumen are correctly segmented, however, some lumen areas are wrongly classified as tubules. This is because the original images contains ring-like lumen in several parts near the center. Here, the shape that lumen takes, resembles with the boundary of an elliptical tubule. Also, many lumen regions are significantly bright, either equal to or even brighter than the tubule boundaries enclosing them. This causes lumen to be wrongly segmented as tubule boundaries. Despite some tubules having small biological mass attached to their walls, they are correctly segmented as a part of tubule boundary with most details preserved. An example image shown in Fig. 5(f), K-IV is more challenging because of very low pixel intensities. In this case, most tubule boundaries in the original image are not clearly observable. Our method is still able to generate an acceptable segmentation, which would be rather difficult to obtain even by a human observer.

Figure 6 shows a few examples of the segmentation results of our proposed method as a visual comparison with that obtained using other segmentation methods for the liver data: L-I, L-II, L-III, and L-IV. As shown in Figs. 6(c)–6(e), our method is able to segment most cell boundaries and highlight the vascular space, generally better than other methods. SteerableJ[39] seems to produce better visual segmentation results than active contour[24] and Squassh[37] and close to the results of our proposed method. Note that each Fig. 6(e) is obtained by doing jelly filling or background labeling on the final segmentation result, as shown in Fig. 6(c). We tuned parameters of other methods to obtain the best results based on our understanding of the method, a reasonable tuning attempts in the spirit of providing an objective comparison of segmentation results obtained using various methods.

We hand-segmented a few images and the segmentation was verified by expert clinician/biologists. We used the hand-segmentation for visual comparison and also as the ground truth to get accuracy, type-I, and type-II errors for each method in the context of segmenting boundaries. Accuracy is obtained as the ratio of number of correctly segmented boundaries and background pixels to the total number of pixels. Type-I error also known as false detection is computed as the ratio of number of background pixels falsely detected as tubule boundaries to the total number of pixels. Type-II error also known as missed detection is computed as the ratio of number of tubule boundaries pixels falsely detected as background to the total number of pixels. Table 2 provides accuracy, type-I and type-II errors for the example image from L-I, L-II, L-III, and L-IV. Among all other comparison methods, Squassh[37] seems to perform the closest to our proposed method. It can be observed that Squassh[37] gives a better accuracy of segmenting boundaries than our proposed method for data L-I. For L-II, it has the same accuracy as that of our proposed method. However, for L-III and L-IV, our proposed method clearly outperforms

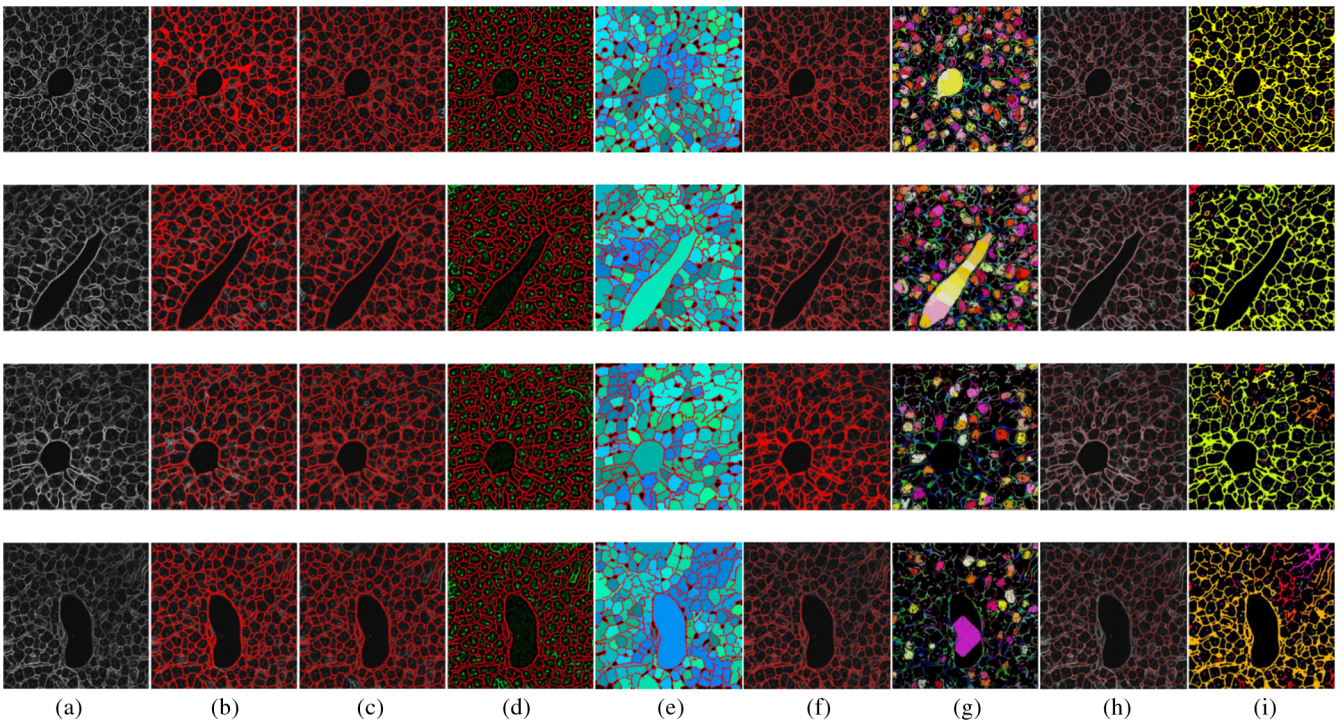

Fig. 6 Visual comparison of segmentation results. Rows (from top to bottom): L-I, L-II, L-III, and L-IV data. (a) Original image, (b) hand-segmentation (used as ground truth), (c–e) our proposed method, (f) SteerableJ,[39] (g) region competition,[34] (h) active contour,[24] and (i) Squassh.[37]

Table 2 Performance comparison of boundary segmentation for liver images from L-I, L-II, L-III and L-IV.

	L-I			L-II			L-III			L-IV		
Method	Acc.	Type-I	Type-II	Acc.	Type-I	Type-II	Acc.	Type-I	Type-II	Acc.	Type-I	Type-II
Active contour[24]	78.8%	0.6%	20.5%	82%	0.7%	17.3%	84.4%	0.9%	14.7%	82.5%	0.9%	16.6%
SteerableJ[39]	82.4%	4.2%	13.4%	84.7%	3.5%	11.8%	85.9%	9.2%	4.9%	83.9%	2.6%	13.5%
Squassh[37]	87.6%	5.4%	7.1%	87.9%	6.7%	5.4%	86.7%	8%	5.3%	85.4%	6.9%	7.7%
Jelly filling	86.5%	4.2%	9.2%	87.9%	5.3%	6.8%	87.9%	6.7%	5.4%	87.5%	5.1%	7.5%

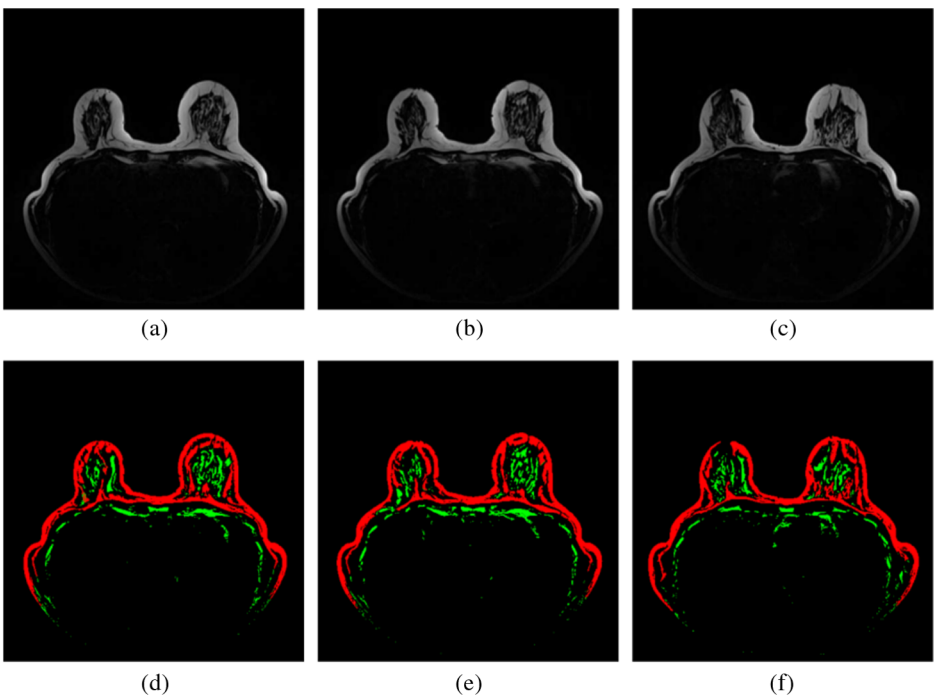

Fig. 7 Segmentation results for M-I-M-IV: (a–c) original mammography images and (d–f) breast and fat tissue segmentation.

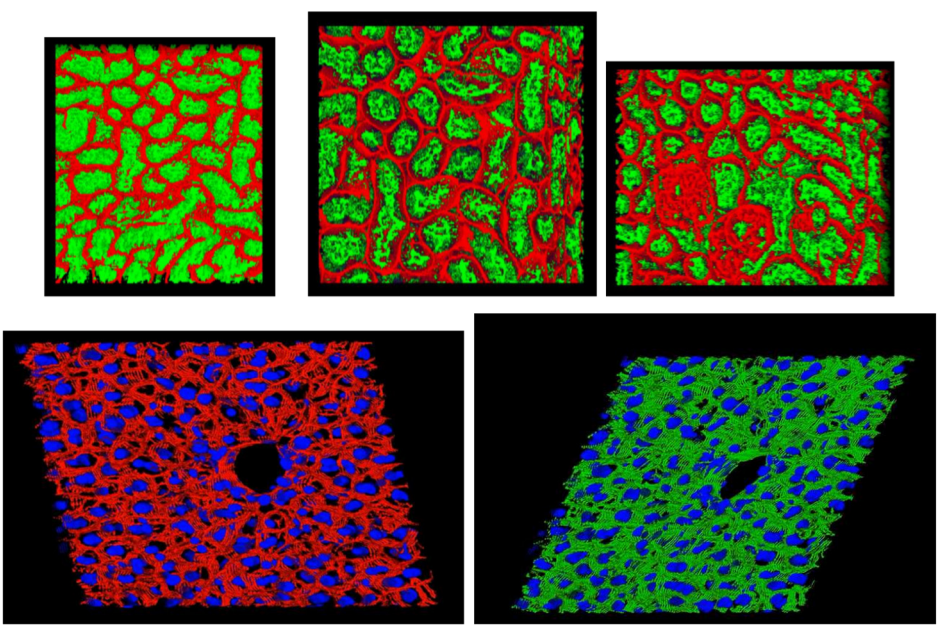

Fig. 8 3-D visualization of different cross-sections of segmentation outcome.

other methods. Active contour and SteerableJ perform worse than our proposed method in terms of accuracy for all tested datasets. Our method has also produced acceptable Type-I and Type-II errors.

Figure 7 depicts examples of segmentation results for M-I-M-IV mammogram images. The breast boundaries and body outline are segmented and shown in red and the tissues inside breasts shown in green. Therefore, our method is also effective in segmenting breasts regions and isolating fat tissues in MRI mammography images.

Some 3-D visualizations of segmentation produced using our method are presented in Fig. 8, using a widely used 3-D visualization tool Voxx.[47] Figures in the top row depict the structure of tubule boundaries (red) and lumen (green) in the kidney. In the top right figure, two glomeruli connected to tubules in the kidney specimen are visible and clearly identifiable. In the bottom row figures, 3-D visualizations of the liver segmentation are presented. The cellular structures that are shown in red in the left image and green in the right image using our proposed method are important structural entities of the liver. Note that the nuclei (shown in blue) are segmented from images representing a different color channel using a separate stochastic point process-based method described in Ref. 38. This demonstrates that our proposed segmentation framework can produce the desired outcome and is useful in characterizing various biological structures and mechanisms.

5 Conclusions and Future Work

In this paper, we described a jelly filling segmentation method for biological images containing multitarget labeling. Intuitively, our proposed method is based on filling disjoint regions of an image with jelly-like fluids to iteratively refine segments that represent separable biological entities. We extended our previous work by developing a motion-compensated z-series function and an improved stopping criterion. We also provided further experimental results for a variety of kidney and liver images collected using intravital microscopy and also DCE-MRI mammograms. The results indicate that our method is capable of segmenting biological entities from microscopy and mammography images. A comparative analysis of various segmentation methods demonstrates that in many cases, our proposed method gives better segmentation outcome both visually and quantitatively. We also provided 3-D visualizations of the results obtained using our segmentation method.

A preliminary analysis using the number of pixel-change and accuracy indicate that our method seems to converge mathematically. A detailed proof of the convergence remains future work. Another future direction is to use the principles of differential geometry to segment multiple shapes. A statistical distance function can be used as a segmentation potential to improve our iterative jelly filling segmentation.

Disclosures

No conflicts of interest, financial or otherwise, are declared by the authors.

Acknowledgments

This work was supported by a George M. O'Brien Award from the National Institutes of Health NIH/NIDDK P30 DK079312. We are grateful to Malgorzata Kamocka, Tarek Ashkar, Sherry Clendenon and James Sluka, Yuan Le, Randall Kroeker, Hal Kipfer, and Chen Lin for providing the image data. We thank Chichen Fu and Seth Winfree for the development of C++ and JAVA-based jelly filling plugins for ImageJ. We also thank David Ho and Soonam Lee for their help in generating the comparison data.

References

1. W. Denk, J. Strickler, and W. Webb, "Two-photon laser scanning fluorescence microscopy," *Science* **248**, 73–76 (1990).
2. F. Helmchen and W. Denk, "Deep tissue two-photon microscopy," *Nat. Methods* **2**, 932–940 (2005).
3. D. Richardson and J. Lichtman, "Clarifying tissue clearing," *Cell* **162**, 246–257 (2015).
4. B. Luck et al., "An image model and segmentation algorithm for reflectance confocal images of in vivo cervical tissue," *IEEE Trans. Image Process.* **14**, 1265–1276 (2005).
5. M. Kyan et al., "Feature extraction of chromosomes from 3-D confocal microscope images," *IEEE Trans. Biomed. Eng.* **48**, 1306–1318 (2001).
6. K. Dunn et al., "Functional studies of the kidney of living animals using multicolor two-photon microscopy," *Am. J. Physiol. Cell Physiol.* **283**, C905–C916 (2002).
7. K. Lorenz et al., "Three dimensional segmentation of fluorescence microscopy images using active surfaces," in *Proc. of the IEEE Int. Conf. on Image Processing*, Melbourne, Australia, pp. 1153–1157 (2013).
8. A. Dufour et al., "Segmenting and tracking fluorescent cells in dynamic 3-D microscopy with coupled active surfaces," *IEEE Trans. Image Process.* **14**, 1396–1410 (2005).
9. N. Gadgil et al., "Jelly filling segmentation of fluorescence microscopy images containing incomplete labeling," in *Proc. of the IEEE Int. Symp. on Biomedical Imaging*, Prague, Czech Republic (2016).
10. K. Lorenz et al., "Digital correction of motion artefacts in microscopy image sequences collected from living animals using rigid and nonrigid registration," *J. Microsc.* **245**, 148–160 (2012).
11. J. Canny, "A computational approach to edge detection," *IEEE Trans. Pattern Anal. Mach. Intell.* 679–698 (1986).
12. C. Harris and M. Stephens, "A combined corner and edge detector," in *Proc. Alvey Vision Conf.*, Manchester, UK, Vol. 15, p. 50 (1988).
13. M. Sezgin and B. Sankur, "Survey over image thresholding techniques and quantitative performance evaluation," *J. Electron. Imaging* **13**, 146–168 (2004).
14. R. Haralick, S. Sternberg, and X. Zhuang, "Image analysis using mathematical morphology," *IEEE Trans. Pattern Anal. Mach. Intell.* 532–550 (1987).
15. J. Serra, "Morphological filtering: an overview," *Signal Process.* **38**, 3–11 (1994).
16. L. Shapiro and G. Stockman, *Computer Vision*, Prentice Hall, Upper Saddle River, New Jersey (2001).
17. M. Kass, A. Witkin, and D. Terzopoulos, "Snakes: active contour models," *Int. J. Comput. Vision* **1**, 321–331 (1988).
18. R. Delgado-Gonzalo et al., "Snakes on a plane: a perfect snap for bioimage analysis," *IEEE Signal Process. Mag.* **32**, 41–48 (2015).
19. V. Caselles, R. Kimmel, and G. Sapiro, "Geodesic active contours," *Int. J. Comput. Vision* **22**, 61–79 (1997).
20. T. Chan and L. Vese, "Active contours without edges," *IEEE Trans. Image Process.* **10**, 266–277 (2001).
21. S. Lankton and A. Tannenbaum, "Localizing region-based active contours," *IEEE Trans. Image Process.* **17**, 2029–2039 (2008).
22. C. Pluempitiwiriyawej et al., "STACS: new active contour scheme for cardiac MR image segmentation," *IEEE Trans. Med. Imaging* **24**, 593–603 (2005).
23. L. Coulot et al., "Topology preserving STACS segmentation of protein subcellular location images," in *Proc. of the IEEE Int. Symp. on Biomedical Imaging*, Arlington, Virginia, pp. 566–569 (2006).
24. B. Li and S. T. Acton, "Active contour external force using vector field convolution for image segmentation," *IEEE Trans. Image Process.* **16**, 2096–2106 (2007).
25. H. Li et al., "Automated actin filament segmentation, tracking and tip elongation measurements based on open active contour models," in *Proc. of the IEEE Int. Symp. on Biomedical Imaging*, Boston, Massachusetts, pp. 1302–1305 (2009).

26. B. Li and S. Acton, "Automatic active model initialization via Poisson inverse gradient," *IEEE Trans. on Image Process.* **17**, 1406–1420 (2008).
27. L. Vincent and P. Soille, "Watersheds in digital spaces: an efficient algorithm based on immersion simulations," *IEEE Trans. Pattern Anal. Mach. Intell.* **13**, 583–598 (1991).
28. M. Velliste and R. Murphy, "Automated determination of protein subcellular locations from 3D fluorescence microscope images," in *Proc. of the IEEE Int. Symp. on Biomedical Imaging*, Washington, DC, pp. 867–870 (2002).
29. V. Grau et al., "Improved watershed transform for medical image segmentation using prior information," *IEEE Trans. Med. Imaging* **23**, 447–458 (2004).
30. K. Keraudren et al., "Two-step watershed segmentation of epithelial cells," in *Proc. of the 6th Int. Workshop on Microscopic Image Analysis with Applications in Biology*, Heidelberg, Germany (2011).
31. L. Vincent, "Morphological grayscale reconstruction in image analysis: applications and efficient algorithms," *IEEE Trans. Image Process.* **2**, 176–201 (1993).
32. J. Sijbers et al., "Watershed-based segmentation of 3D MR data for volume quantization," *Magn. Reson. Imaging* **15**(6), 679–688 (1997).
33. G. Srinivasa et al., "Active mask segmentation of fluorescence microscope images," *IEEE Trans. Image Process.* **18**, 1817–1829 (2009).
34. J. Cardinale, G. Paul, and I. F. Sbalzarini, "Discrete region competition for unknown numbers of connected regions," *IEEE Trans. Image Process.* **21**, 3531–3545 (2012).
35. P. Quelhas et al., "Cell nuclei and cytoplasm joint segmentation using the sliding band filter," *IEEE Trans. Med. Imaging* **29**, 1463–1473 (2010).
36. A. Narayanaswamy et al., "Robust adaptive 3-D segmentation of vessel laminae from fluorescence confocal microscope images and parallel GPU implementation," *IEEE Trans. Med. Imaging* **29**, 583–597 (2010).
37. G. Paul, J. Cardinale, and I. F. Sbalzarini, "Coupling image restoration and segmentation: a generalized linear model/Bregman perspective," *Int. J. Comput. Vision* **104**, 69–93 (2013).
38. N. Gadgil et al., "Nuclei segmentation of fluorescence microscopy images based on midpoint analysis and marked point process," in *Proc. of the IEEE Southwest Symp. on Image Analysis and Interpretation*, Santa Fe, New Mexico, pp. 37–40 (2016).
39. M. Jacob and M. Unser, "Design of steerable filters for feature detection using Canny-like criteria," *IEEE Trans. Pattern Anal. Mach. Intell.* **26**, 1007–1019 (2004).
40. G. Carneiro et al., "Review of deep learning methods in mammography, cardiovascular, and microscopy image analysis," in *Deep Learning and Convolutional Neural Networks for Medical Image Computing*, Springer, Cham, Switzerland, pp. 11–32 (2017).
41. H. Chen et al., "DCAN: deep contour-aware networks for accurate gland segmentation," in *Proc. of the IEEE Conf. on Computer Vision and Pattern Recognition*, Seattle, Washington, pp. 2487–2496 (2016).
42. O. Kraus, J. Ba, and B. Frey, "Classifying and segmenting microscopy images with deep multiple instance learning," *Bioinformatics* **32**, i52–i59 (2016).
43. J. Watt, R. Borhani, and A. Katsaggelos, *Machine Learning Refined: Foundations, Algorithms, and Applications*, Cambridge University Press, Cambridge, United Kingdom (2016).
44. Y. Le et al., "Development and evaluation of TWIST Dixon for dynamic contrast-enhanced (DCE) MRI with improved acquisition efficiency and fat suppression," *J. Magn. Reson. Imaging* **36**, 483–491 (2012).
45. C. Giardina and E. Dougherty, *Morphological Methods in Image and Signal Processing*, Prentice Hall Inc., Engelwood Cliffs, New Jersey (1988).
46. M. D. Abràmoff, P. J. Magalhães, and S. J. Ram, "Image processing with ImageJ," *Biophotonics Int.* **11**, 36–42 (2004).
47. J. Clendenon et al., "Voxx: a PC-based, near real-time volume rendering system for biological microscopy," *Am. J. Physiol. Cell Physiol.* **282**, C213–C218 (2002).

Neeraj J. Gadgil received his BE (Hons) in electrical and electronics engineering from Birla Institute of Technology and Science (BITS) Pilani, India, in 2009, and PhD in electrical and computer engineering from Purdue University, West Lafayette, Indiana. His research interests are image/video processing and statistical image analysis/segmentation for biomedical applications.

Paul Salama received his PhD in electrical engineering from Purdue University in 1999. In 1999, he joined the Department of Electrical and Computer Engineering, in the Purdue School of Engineering and Technology, at Indiana University-Purdue University Indianapolis, Indianapolis, Indiana, where he is currently a professor of electrical and computer engineering and the associate dean for graduate programs within the school. His research interests include image analysis, image and video compression, machine learning, statistical signal processing, and medical imaging. He is a senior member of IEEE and member of SPIE.

Kenneth W. Dunn received his PhD in biology from SUNY Stony Brook in 1986. He then took a position as an NIH postdoctoral fellow at Columbia University. In 1995, he joined the faculty in the Department of Medicine at Indiana University and was promoted to full professor in 2014. His research is broadly focused on the development and application of methods of microscopy, particularly intravital microscopy to the study of cell biology and physiology.

Edward J. Delp is currently the Charles William Harrison distinguished professor of electrical and computer engineering and a professor of biomedical engineering at Purdue University. His research interests include image and video compression, multimedia security, medical imaging, multimedia systems, communication and information theory. He has published and presented more than 500 papers. He is a fellow of IEEE, a fellow of SPIE, a fellow of the Society for Imaging Science and Technology (IS&T), and a fellow of the American Institute of Medical and Biological Engineering.